

Characterization of LiBH₄–MgH₂ Reactive Hydride Composite System with Scattering and Imaging Methods Using Neutron and Synchrotron Radiation

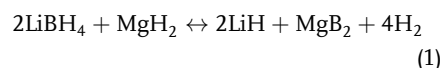
Fahim Karimi,* Stefan Börries, P. Klaus Pranzas, Oliver Metz, Armin Hoell, Gökhan Gizer, Julián A. Puszkiel, Maria V. C. Riglos, Claudio Pistidda, Martin Dornheim, Thomas Klassen, and Andreas Schreyer

Reversible solid-state hydrogen storage in metal hydrides is a key technology for pollution-free energy conversion systems. Herein, the LiBH₄–MgH₂ composite system with and without ScCl₃ additive is investigated using synchrotron- and neutron-radiation-based probing methods that can be applied to characterize such lightweight metal–hydrogen systems from nanoscopic levels up to macroscopic scale. Combining the results of neutron- and photon-based methods allows a complementary insight into reaction paths and mechanisms, complex interactions between the hydride matrix and additive, hydrogen distribution, material transport, structural changes, and phase separation in the hydride matrix. The gained knowledge is of great importance for development and optimization of such novel metal-hydride-based hydrogen storage systems with respect to future applications.

1. Introduction

Reversible solid-state hydrogen storage in metal hydrides offers high volumetric and gravimetric densities combined with a high degree of safety. The so-called reactive hydride composite (RHC) systems are a special class of solid-state hydrogen storage materials that are promising for mobile applications. The concept of RHCs is to build mixtures of metal hydrides that can mutually react over the dehydrogenation process, thereby lowering the overall reaction enthalpy of the system.^[1] In this work, the so-called lithium-based

RHC 2LiBH₄ + MgH₂ (Li-RHC) is investigated, in detail, which can reversibly store 11.5 wt.% hydrogen via the reaction




with a theoretical reaction enthalpy of 46 kJ mol⁻¹ H₂.^[1] Due to its sluggish reaction kinetics, a small amount of ScCl₃ was used, which could improve the dehydrogenation/hydrogenation reaction kinetics of the Li-RHC system by an order of magnitude. For an optimized scale-up, aiming at future industrial applications, detailed knowledge about, both, nanoscopic and macroscopic structures of this composite system is mandatory. Therefore, samples at the lab scale as

well as at the macroscopic range were investigated using synchrotron and neutron irradiation facilities. For probing the nanostructure of the system, scattering, diffraction, and absorption techniques were used, whereas neutron radiography and tomography methods were applied to resolve the spatial distribution of hydrogen content on the macroscopic level inside an operating metal hydride tank. The combined nanoscopic and macroscopic results reveal fascinating new insights on the fundamental properties of the Li-RHC system, which are of great importance for future scale-up systems in terms of application.

F. Karimi, S. Börries, P. K. Pranzas, O. Metz, G. Gizer, J. A. Puszkiel, M. V. C. Riglos, C. Pistidda, M. Dornheim, T. Klassen
Zentrum für Material- und Küstenforschung
Helmholtz-Zentrum HEREON
Max-Planck-Straße 1, Geesthacht D-21502, Germany
E-mail: fahim.karimi2017hh@gmail.com

A. Hoell
Helmholtz-Zentrum Berlin für Materialien und Energie
Hahn-Meitner-Platz 1, Berlin D-14109, Germany

 The ORCID identification number(s) for the author(s) of this article can be found under <https://doi.org/10.1002/adem.202100294>.

© 2021 The Authors. Advanced Engineering Materials published by Wiley-VCH GmbH. This is an open access article under the terms of the Creative Commons Attribution License, which permits use, distribution and reproduction in any medium, provided the original work is properly cited.

DOI: 10.1002/adem.202100294

J. A. Puszkiel
Department of Physicochemistry of Materials
Consejo Nacional de Investigaciones Científicas y Técnicas (CONICET) y
Centro Atómico Bariloche
Av. Bustillo km 9500, S.C. de Bariloche, Argentina

M. V. C. Riglos
Department of Metalphysics
Consejo Nacional de Investigaciones Científicas y Técnicas (CONICET) y
Centro Atómico Bariloche
Av. Bustillo km 9500, S.C. de Bariloche, Argentina

A. Schreyer
European Spallation Source
ERIC Box 176, Lund S-22100, Sweden

2. Results and Discussion

2.1. Characterization of Metal-Hydride Material

The result of in situ SR-XPD measurements of LiRHC + 0.1ScCl₃ is shown in Figure 1. At room temperature, the as-milled material consists of LiBH₄, MgH₂, ScCl₃, and LiCl. The presence of ScCl₃ and LiCl in the starting material indicates a partial reaction between LiBH₄ and ScCl₃ already during the milling procedure. After heating the sample to about 115 °C, the phase transformation of LiBH₄ from room temperature orthorhombic *o*-LiBH₄ phase to high-temperature hexagonal *h*-LiBH₄ phase is detected. At temperatures of roughly 280 °C the diffraction peaks of LiBH₄, ScCl₃, and LiCl disappear simultaneously, which can be inferred to melting of LiBH₄ and a possible reaction between these products. The metallic phase of Mg appears at around 350 °C accompanied by decreasing intensities of MgH₂. This can be correlated to the first dehydrogenation reaction of the composite system.

Around 380 °C, the diffraction peaks of the MgB₂ phase start to appear while the Bragg peaks of Mg decline. This can be attributed to the reaction between metallic Mg and the liquid LiBH₄ phase resulting in the final reaction products LiH and MgB₂. However, no scandium-containing phases are observed as an intermediate or a final product via in situ SR-XPD. To reveal the chemical state of scandium in the samples, the EXAFS part of the XAS spectra was extracted and Fourier transformed (FT) to visualize the radial atomic distribution (RAD) around the

resonant atom (Sc). Also, the EXAFS spectrum of the ScCl₃ as a reference sample was FT and plotted in Figure 2.

The RAD of the as-milled sample and ScCl₃ reference show some similarities in the first coordination shell, and clear differences in the second coordination shell. After the first desorption, the local environment of Sc has changed entirely (in comparison to the local environment of the ScCl₃ reference sample) and remains stable upon further hydrogenation cycling. First-principles calculations of the first and second coordination shells of the cycled samples are well reproduced by ScB₂ (with the hexagonal crystal structure, the space group P6/mmm, and the COD ID 1 510 831). The first experimental RAD amplitude is reproduced by Sc atoms in the coordination shell of ScB₂ and the second experimental RAD amplitude is reproduced by a superposition of the calculated amplitudes of boron and scandium located in the second coordination shell of ScB₂. Therefore, it can be concluded that the chemical state of scandium in the as-milled system is a superposition of Sc³⁺ and Sc²⁺, which is transformed fully to Sc²⁺ in the cycled state and remains stable upon further cycling. This indicates that ScCl₃ reacted with LiBH₄ to form ScB₂ and LiCl. Therefore, the disappearance of the Cl element can be attributed to the formation of LiCl, which remains stable as an inert material over the cycles, which is in agreement with the in situ SR-XPD results of the as-milled sample (Figure 1). The local environment of Sc can be concluded to be ScB₂, and it remains stable after its formation over the cycling procedure. This result is in good agreement with results obtained in previous studies.^[2] To determine the size distribution of ScB₂

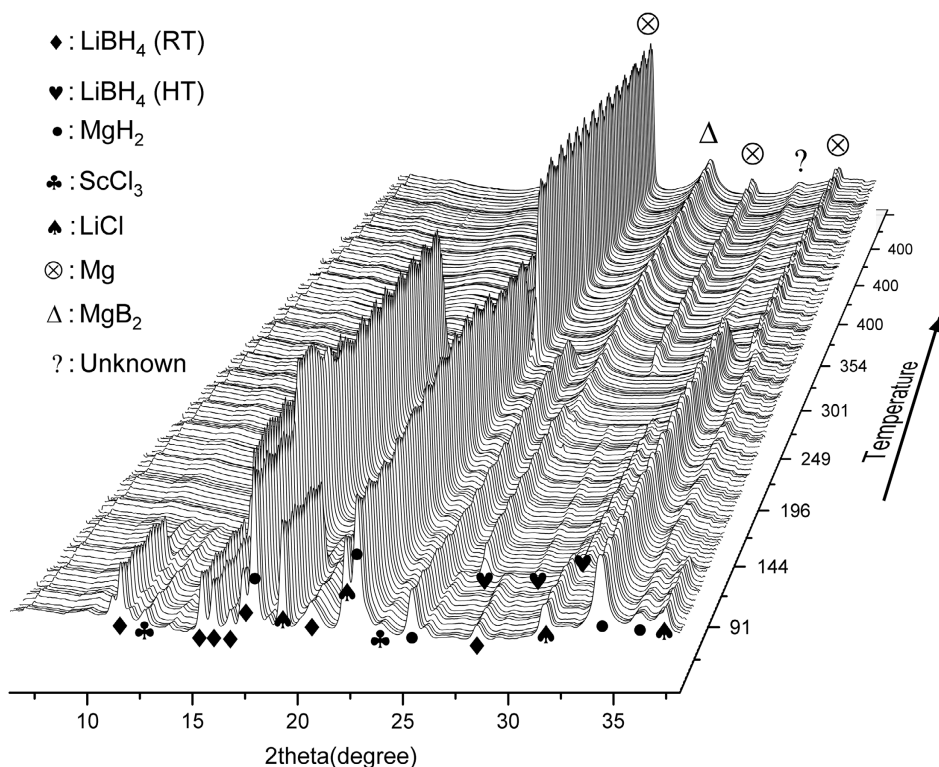


Figure 1. Dehydrogenation reaction of $2\text{LiBH}_4 + \text{MgH}_2 + 0.1\text{ScCl}_3$ observed by in situ SR-XPD. The sample was kept at 4 bar H₂ backpressure while the temperature ramp was set to 3 °C min⁻¹ and was heated from RT to 400 °C. Data collection continued at isothermal conditions after reaching 400 °C.

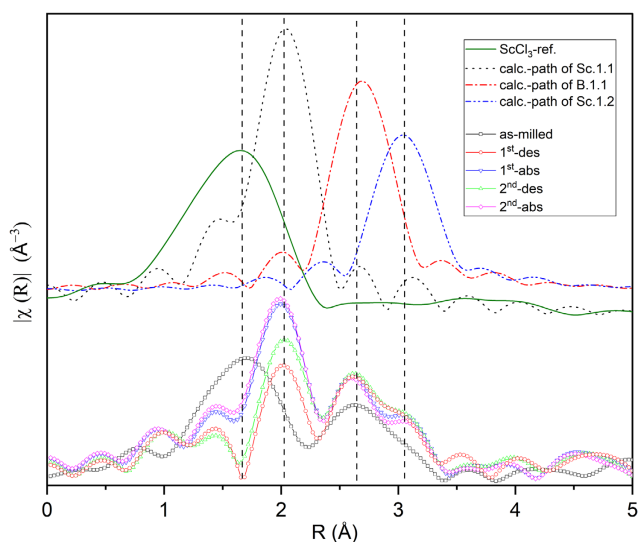


Figure 2. Fourier-transformed EXAFS patterns (radial atomic distributions (RADs)) of Sc in the hydride matrix at different hydrogenation states are shown in the lower part of the figure, and the RAD patterns of ScCl_3 and the calculated RAD amplitudes from the first and second shell of the hexagonal (P6mm) ScB_2 phase are displayed in the upper part of the figure.

particles, ASAXS measurements were conducted. Using the anomalous dispersion of the scattering amplitudes close to the X-ray absorption edges of elements in the sample, ASAXS offers element-specific averaged structural information on the nanometer scale. From the ASAXS scattering curves, using the method described by Stuhrmann,^[3] the pure resonant scattering curves were isolated. An exemplary result of a resonant scattering curve with its corresponding fit, the mixed resonant curve, and the total scattering curve is shown in **Figure 3**.

Distance distribution functions (DDFs) of ScB_2 particles were calculated from the pure resonant scattering curves; the DDF for all samples are shown in **Figure 4**. The average ScB_2 particles are

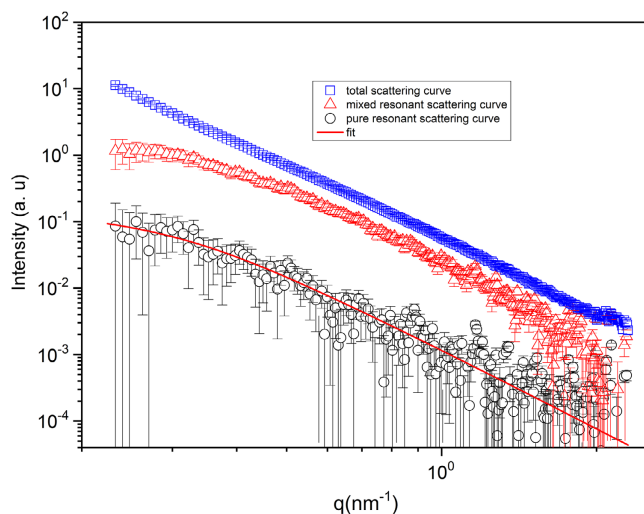


Figure 3. Total scattering curve (blue squares), mixed resonant scattering curve (red triangles), and pure resonant scattering curve (black circles) of as-milled sample and its corresponding model fit (red line).

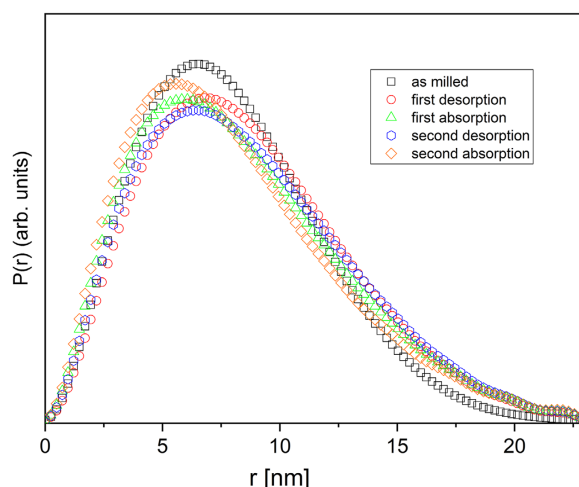


Figure 4. Distance-distribution functions of ScB_2 particles in $2\text{LiBH}_4 + \text{MgH}_2 + 0.1\text{ScCl}_3$ samples at different hydrogenation states.

around 6 nm in size, whereas the maximum sizes are roughly 20 nm. These results are in agreement with the recent reports on such systems.^[4]

The average, as well as the maximum size distribution of ScB_2 particles do not change significantly overall, only a small coarsening effect is visible at larger sizes. This shows the stable nanostructure over dehydrogenation/hydrogenation cycling, which is crucial for the degree of catalytic activity of the additive. However, the degree of crystallinity of all ScB_2 particles increases with the cycling procedure, as can be deduced from the increasing experimental EXAFS amplitudes of the samples (Figure 2). As ScB_2 has the same crystal structure as MgB_2 , it can act as a nucleation agent for MgB_2 . Indeed, ScB_2 provides two nucleation sites for MgB_2 — $\text{Sc}\{1011\}/\text{MgB}_2\{1011\} = 1.1$; $\text{Sc}\{1010\}/\text{MgB}_2\{1010\}$ —with a mismatch of 1.1 and 1.9, respectively. Therefore, the ScB_2 nanoparticles can indeed have some structural effects on their surrounding hydride matrix. Therefore, SANS/USANS measurements were conducted to examine the size distribution of the hydride matrix for Li-RHC with and without ScCl_3 additive, respectively. The results of this investigation are shown in **Figure 5**. It should be mentioned that in the samples for these measurements ^7Li , ^{11}B , and D isotopes were used to minimize their respective incoherent neutron scattering. The SANS/USANS scattering curves were corrected for multiple scattering and instrumental smearing and merged subsequently. Thereafter, SANS-USANS curves were fitted assuming hard spherical structures and the calculated size distributions are shown in the inset figure in Figure 5.

A comparison between the two scattering curves shows that the scattering curve of the doped sample has a more pronounced shoulder in the Porod region at about 0.5 nm^{-1} , which indicates a relatively high number of smaller structures at the nanoscale in this system. Indeed, this is confirmed by the calculated size distribution of the sample doped with ScCl_3 , where the volume fraction of structures in the range of about 1–100 nm is significantly higher in comparison to the undoped sample. In contrast, in the Guinier region of the doped sample the scattering curve shows a smaller shoulder compared to the pure system. This indicates a much lower number of big particles in the doped system, which

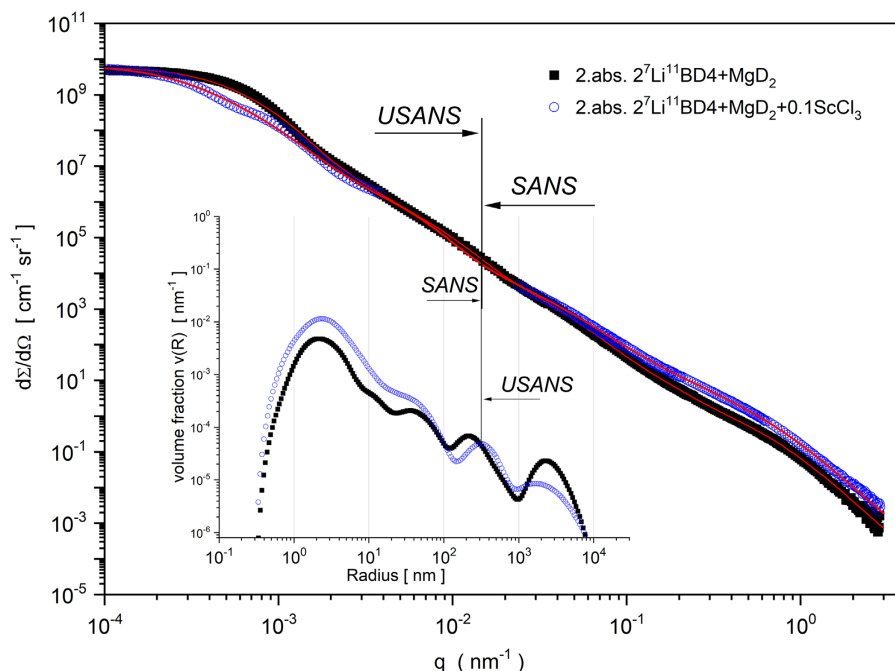


Figure 5. Merged SANS and USANS curves of the doped Li-RHC + 0.1ScCl₃ and pure Li-RHC samples after the second absorption with deuterium. In the inset figure, the corresponding calculated size distributions are displayed assuming a spherical particle model.

is confirmed by the calculated size distribution in the range of 1–10 μm. This shows that the additive serves as a grain refiner in the milling process, leading to smaller nanostructures in the metal hydride matrix. However, the maximum particle sizes in both samples are comparable. These results are summarized in a sketch in **Figure 6**.

As can be assumed, based on the EXAFS and ASAXS results, there is a nanoscopic size distribution of ScB₂ particles (illustrated as small (blue) squares in Figure 6), which can provide abundant nucleation sites for nucleation and growth of the

MgB₂ phase. In contrast, in the pure Li-RHC system a higher energy barrier has to be overcome to create a stable MgB₂ nucleus. Therefore, it can be concluded that ScB₂ nanoparticles most likely act as nucleation agents that significantly reduce the energy barrier for nucleation and growth of MgB₂. Indeed, this implies the dehydrogenation/hydrogenation reaction to occur around ScB₂ nanoparticles, resulting in much smaller matrix structures for the doped Li-RHC system in comparison to the pure one. These smaller nanostructures result in a much larger reaction surface area and shorter diffusion paths, in comparison

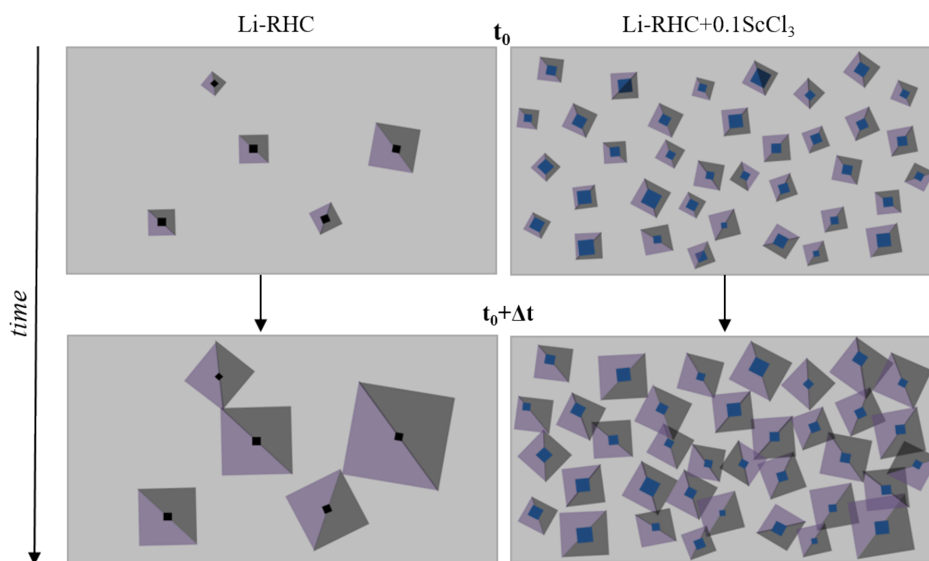


Figure 6. Illustration demonstrating the reason for different kinetics in phase growth of MgB₂ in pure and doped Li-RHC systems, respectively.

to the pure Li-RHC. This not only facilitates the desorption process but also significantly improves the hydrogenation process because the MgB_2 phase is much more evenly and finely distributed in the LiH phase, and therefore has a considerably larger reaction surface area, which is crucial for the rehydrogenation of this composite system, as pointed out by Le et al.^[5] and other investigations^[6] (see also reaction 1). Therefore, the reduced energy barrier is most likely the reason for the faster kinetics of the system with additive. In the next step this composite system was scaled up. A tank was filled with the Li-RHC material to investigate the macroscopic properties of the system for possible on-board applications by using neutron radiography and tomography methods.

2.2. Neutron Imaging Studies of Hydrogen Storage Tank Systems

In **Figure 7a** an overview image of the so-called “FlexiStore” tank is plotted for reconstructed data corresponding to the desorbed state of Li-RHC. The volume data were cut to visualize the inner part of the tank containing the Li-RHC pellet.

In **Figure 7b** the pellet is extracted as the region of interest. Here, the distribution of the voxel attenuation coefficient μ_{voxel} of the reconstructed combined data is shown, representing the spatial distribution of the attenuation coefficient with respect to hydrogen content. **Figure 7c** shows the corresponding histogram, with voxel attenuations sorted into $(2)^{16}$ equally distributed bins in the region of $[0, \mu_{\text{max}}]$. For the quantification of hydrogen distribution in the material inside the tank, a novel normalization procedure is applied in this work extending the 2D normalization procedure case^[7–9] for the 3D case. This approach considers the overall voxels of the image, and the hydrogen content in each

voxel is normalized by the corresponding material mass (for the data set of desorbed state the total mass of the pellet is used). The resulting quantitative distribution of hydrogen contents in the pellet is visualized in **Figure 8**.

In **Figure 8a**, the total pellet volume is shown. Here, as indicated by the color-coded bar, the hydrogen content reaches values up to 20 wt% H_2 located in the lower left area of the pellet, whereas in the remaining area the corresponding values are significantly lower. Thus, a combined tomography analysis of the hydrogenated and dehydrogenated state confirms the motion of the material in the presence of hydrogen pseudocontents to be higher than the maximal theoretical capacity. In **Figure 8b**, the threshold for calculating the volume data set is selected such that all spatial distributions of hydrogen content are equal or above 9 wt% H_2 . As can be seen, the location of voxels is predominantly in the aforementioned lower left part of the pellet volume, indicating no limitation to the surface. From this, it can be deduced that the directed mass transport by motion of LiBH_4 toward the lower left pellet boundary is equally distributed in the axial pellet direction. This indicates that capillary forces are causing the motion of the liquid LiBH_4 to minimize the surface energy by wetting of the solid matrix framework. The high pseudocontents of hydrogen could be caused by a directed motion of the LiBH_4 phase toward an optimal material-packing density providing an ideal porous framework for agglomeration and wetting, thus attracting mass transport of LiBH_4 . The distribution of the material packing density in the pellet is essentially determined by the compaction process itself. In the first approximation, the packing density is homogeneous perpendicular toward the axis of compaction, which is the axial direction of the pellet. Accordingly, a homogeneous distribution of LiBH_4 along the axial pellet direction is expected because it exhibits

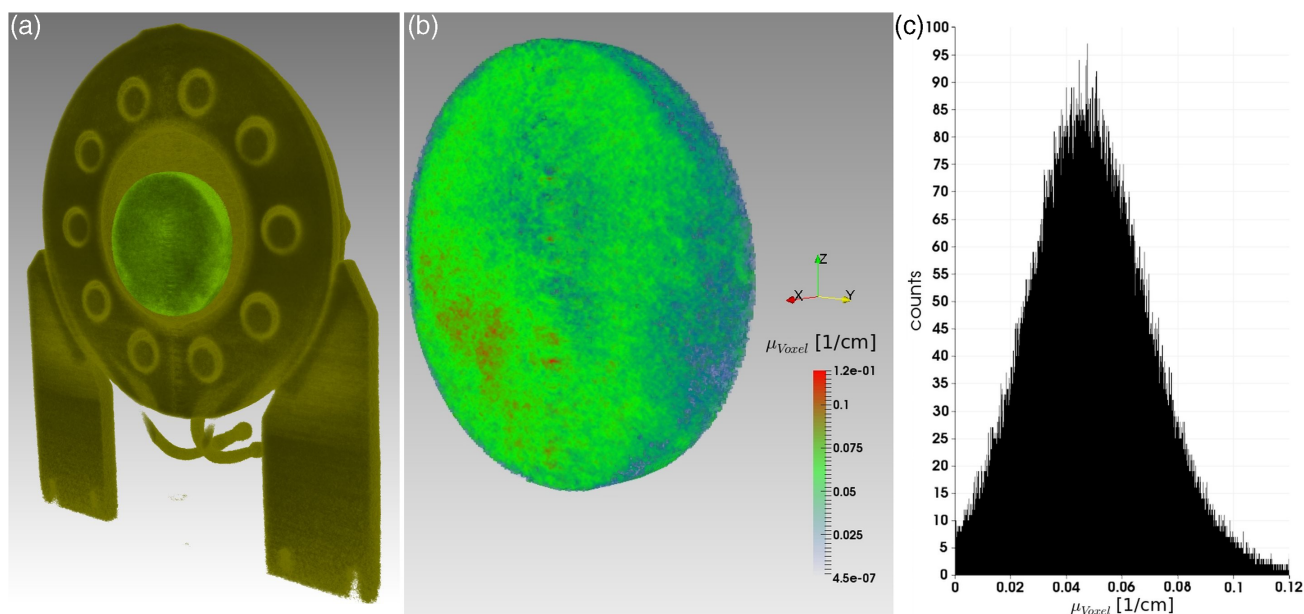


Figure 7. a) Overview image of reconstructed data of the FlexiStore tank showing the tank geometry, cut to visualize the metal hydride pellet in the tank center with the Li-RHC material in the desorbed state. Visualization of data was done with VGStudio Max.^[21] b) The spatial distribution of voxel attenuation coefficients for the pellet region of interest of the combined data set is shown, quantitatively scaled by pseudocolors, and c) the corresponding histogram of the voxel attenuation coefficient is displayed.

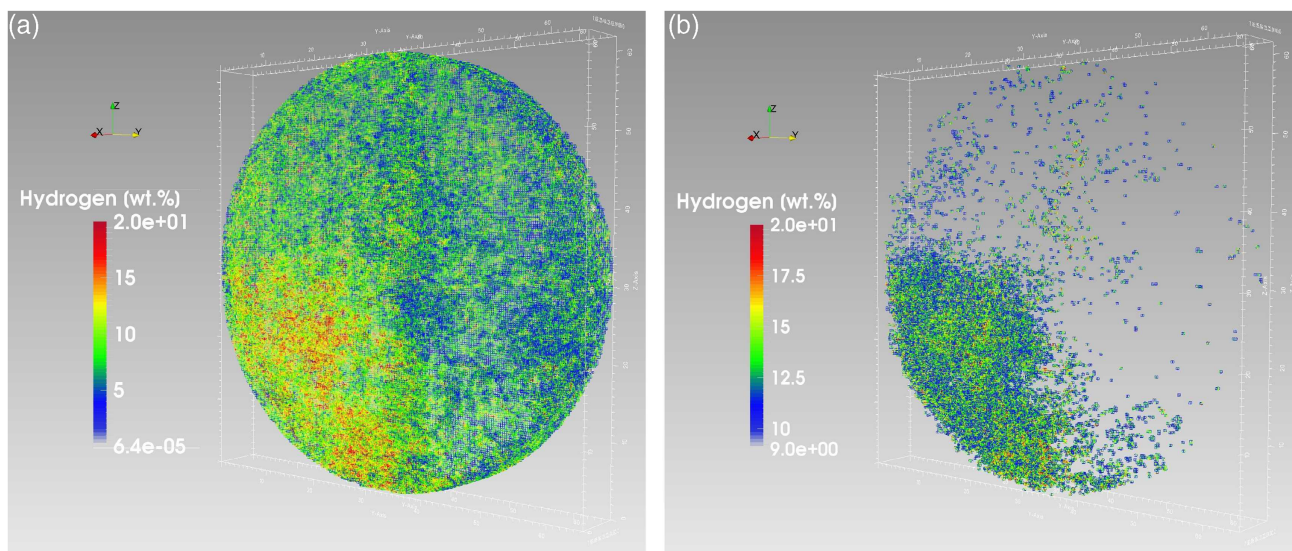


Figure 8. Volume data set for the spatial distribution of the normalized hydrogen content, scaled by pseudocolors. a) Full volume data set and b) a threshold is applied, showing only voxels with corresponding normalized hydrogen content ≥ 9 wt% H_2 .

the same packing density and provides the same porous framework. Based on these results, the following mechanism for the absorption process of scaled-up Li-RHC compacts is proposed: with the beginning of hydrogenation, the system composition is predominantly pure solid state; therefore, it can be stated in general for solid-solid systems that lower packing density and increased porosity enhance the reaction kinetics. In addition, there is a positive correlation of kinetics and temperature, where the latter contributed to, e.g., enhanced diffusion and permeation rates. With further proceeding hydrogen absorption, the amount of liquid $LiBH_4$ phase is continuously increasing, accompanied by an induced motion that is driven by capillary forces present for the porous solid framework due to surface energy minimization and wetting of solid phases. The wettability of the system is assumed to be decent as no macroscopic expulsion of the liquid phase could be observed. The present porous framework in the pellet is inversely related to the material packing density that is defined by the compaction pressure during pellet manufacture. Capillary forces are inversely correlated to pore diameters^[10,11]; hence, areas of maximal attraction are areas of highest packing density. However, the total amount that can accumulate within these areas is limited. Ongoing absorption and a further increasing amount of liquid $LiBH_4$ lead to a partial expulsion of excess $LiBH_4$ out of areas with high packing densities. The optimal porous framework that provides the best compromise of free volume and capillarity is determined to exhibit a packing density range of $[0.75\text{--}0.95]$ $g\text{ cm}^{-3}$, which seems to provide the best porous framework for agglomeration and wetting. This is reasonable because it coincides with the maximal theoretical packing density of the absorbed state, which is 0.83 g cm^{-3} for the given system composition based on solid material compounds. In the final absorption state an accumulation of $LiBH_4$ is observed at the mentioned packing densities. The motion of $LiBH_4$ during the absorption process occurs over long distances of at least 5 mm and affects at least about 1% of the total material. The

material transport within the pellet is an expression of a long-range phase separation process. The reversibility of material transfer during the desorption reaction is questionable due to the long-range motion distances. The observed phase separation is most likely the reason for the degradation of the hydrogen capacity over the cycling procedure as reported by Jepsen et al.^[12] Though material transfer and liquid phase are present, no macroscopic structure loss is observed. Thus, after the initial compaction process, the solid compounds (consisting predominantly of magnesium hydride) seem to form a stable framework during the hydrogen sorption processes that provides sufficient porosity for agglomeration and motion of the liquid $LiBH_4$ phase.

3. Conclusion

In this work, the solid-state hydrogen storage composite system $LiBH_4\text{--}MgH_2$ was studied using synchrotron and neutron radiation research facilities. At the first stage, the hydride material was characterized at the nanoscopic scale up to the micron range, and at the second stage it was scaled up and probed at the macroscopic level in a real hydrogen tank system. The scattering experiments revealed comprehensive information about the reaction mechanism of the system, chemical state, local environment, and size distribution of the used catalyst as well as the size distribution of the matrix structures. A model was developed demonstrating the formation of ScB_2 nanoparticles with a stable nanostructure serving as grain refiner and acting as nucleation agent, providing nucleation sites and reducing the energy barrier for nucleation and growth of the MgB_2 phase. The resulting smaller nanostructures result in a larger surface area and shorter diffusion pathways. This explains the faster kinetics of the Li-RHC system with the additive.

Using neutron radiography and tomography, melting processes, phase separation, and mass transport were characterized inside an operating tank system on the macroscopic level. The

macroscopic phase separation, due to liquefaction of LiBH_4 , was inferred to be the most probable cause for declining hydrogen storage capacity of the tank system over the cycling procedure. Furthermore, the driving forces for the macroscopic motion of the LiBH_4 liquid phase were studied, which led to an optimal material packing density of $[0.75\text{--}0.95] \text{ g cm}^{-3}$, providing an ideal porous framework for agglomeration and wetting during the absorption process. The gained knowledge from this study is of great importance to develop and optimize hydrogen storage materials, which can eventually lead to hydrogen storage tank systems with high capacity and fast kinetic properties for possible mobile applications in the near future.

4. Experimental Section

The raw materials were purchased from Sigma-Aldrich (purity: $\text{LiBH}_4 \geq 98.0\%$, $\text{MgH}_2 \geq 95.0\%$) and Alfa-Aesar ($\text{ScCl}_3 \geq 99.0\%$), and the isotope-containing materials (${}^6\text{Li}^{11}\text{BH}_4$ and ${}^7\text{Li}^{11}\text{BH}_4$ with purities of $\geq 95\%$) were purchased from KAT-Chem Ltd. A high-energy Spex 8000 mL/shaker was used to mill the $\text{LiBH}_4\text{--MgH}_2$ system. The Spex mill was placed in a glove box (BRAUN, company) with purified argon atmosphere ($\text{O}_2 < 10 \text{ ppm}$ and $\text{H}_2\text{O} < 10 \text{ ppm}$). The milling vial and balls were made of stainless steel. The ball-to-powder ratio was chosen to be 10:1.

Diffraction, Scattering, and X-Ray Absorption Techniques: To investigate the crystalline phase of the hydride composite system in situ synchrotron radiation powder diffraction (in situ SR-XPD) measurements were conducted at the beamline I711 at MAX-lab, Lund (Sweden). The incident photon wavelength was set to about $\approx 0.1 \text{ nm}$, and a MarCCD-165 area detector was used to collect the diffracted intensities. All samples were inserted into (single-crystal) sapphire capillaries with an outer diameter of 1.0 mm and a length of 60 mm. The loaded sample holder was taken to the experimental station and attached to a Newport kappa 4-circle diffractometer, using a goniometer head. The sample was kept under 4 bar of H_2 and heated at a rate of $3 \text{ }^\circ\text{C min}^{-1}$ by a ceramic oven placed underneath the capillary while a thermocouple measured the sample temperature positioned close to the sample inside the capillary and controlled via a PID regulator.^[13] X-ray absorption spectroscopy (XAS) measurements were conducted at the D-beamline, at DORIS III, DESY, Hamburg (Germany). The samples were pressed into pellets of 5 mm in diameter and were kept between Kapton tapes. All XAS measurements were conducted in transmission and fluorescence mode. The XAS scans were collected in the energy range 4350–4950 eV, covering the X-ray absorption near-edge structure (XANES) and the extended X-ray absorption fine structure (EXAFS). Anomalous small-angle X-ray scattering (ASAXS) measurements were performed at the 7T-MPW beamline at the synchrotron radiation facility BESSY II (HZB, Berlin, Germany).^[14,15] A multiwire proportional counter gas detector ($20 \times 20 \text{ cm}^2$ in size) was used to measure the scattering intensities. Two sample-to-detector distances were selected ($D_{\text{min}} = 800 \text{ mm}$ and $D_{\text{max}} = 1500 \text{ mm}$) to cover the maximum q -range. Here, q represents the scattering vector, which is defined by $q = (4\pi/\lambda) \sin \theta$, where 2θ is the scattering angle and λ represents the wavelength of the incident photons. The ASAXS intensities were measured at three different energies (4300, 4473, and 4483 eV) below the K-absorption edge of scandium (4492.8 eV). The scattering intensities were corrected for dark current, detector response, sample transmission, and instrumental background. Using precalibrated $90 \text{ }\mu\text{m}$ glassy carbon and silver behenate standards, the intensity and the scattering vector were normalized to an absolute scale. The resonant scattering curves of Sc structures were obtained using the method described by Goerigk et al.^[16] Distance distributions were calculated by fitting the resonant scattering curves using the fit program GNOM.^[17] Small-angle neutron scattering (SANS) and ultra-small-angle neutron scattering (USANS) experiments were performed at the instrument SANS-2 and at the double crystal diffractometer (DCD) of the Geesthacht Neutron Facility (GeNF),

respectively. For SANS measurements, the sample to detector distance SDD was set to four defined values (1, 3, 9, and 21 m). For all four SDDs, the wavelength was set to 0.58 nm, and only for 21 m the samples were measured with the wavelength of 1.16 nm to cover the maximum accessible q -range. The scattering intensities were corrected for sample transmission and detector response and normalized by monitor counts. The scattering intensities were set further to absolute values using a vanadium standard. The USANS measurements were conducted with a wavelength of 0.443 nm. For SANS and USANS experiments, all samples were measured in quartz cuvettes with a thickness of 1 mm. Prior to merging SANS and USANS scattering curves, the USANS scattering curves were further corrected for multiple scattering.^[18,19] Subsequently, the SANS/USANS scattering curves were merged to reveal the entire matrix structures present in the samples extending from nanocrystals up to particles in the micron range.

Neutron Radiography and Tomography Investigations: In situ absorption studies using neutron tomography were performed at the fission neutron imaging instrument NECTAR at FRM II at the Heinz Maier-Leibnitz Zentrum (MLZ) in Garching. First, the desorbed state was characterized to derive the 3D material distribution and packing density. After the absorption process, again, a tomography analysis was performed. Both studies were conducted at room temperature without thermal insulation at a hydrogen pressure of 2 bar. The same measurement parameters were used for both tomography measurements for comparability. In total, for each tomography 375 projections were acquired with corresponding projection angles distributed over 360° and with an exposure time of 120 s. No effect of thermal expansion has to be considered due to the ex situ, room temperature state of the system in desorbed and absorbed conditions. Hence, projection data sets can be combined directly and the ratio of intensity distributions (normalized by the flat field and corrected for the dark image) for the absorbed and desorbed state was computed for every projection step. The projection data were reconstructed using the software OCTOPUS^[20] to derive the attenuation difference caused by hydrogen absorption.

Acknowledgements

Open access funding enabled and organized by Projekt DEAL.

Conflict of Interest

The authors declare no conflict of interest.

Data Availability Statement

Research data are not shared.

Keywords

hydrogen storage materials, imaging, neutrons, scattering methods, synchrotron radiation

Received: March 11, 2021

Revised: July 5, 2021

Published online: August 21, 2021

- [1] a) J. J. Vajo, S. L. Skeith, F. Mertens, *J. Phys. Chem. B* **2005**, *109*, 3719; b) G. Barkhordarian, T. Klassen, M. Dornheim, R. Bormann, *J. Alloys Compd.* **2007**, *440*, L18; c) J. Puzskiel, A. Gasnier, G. Amica, F. Gennari, *Molecules* **2020**, *25*, 163; d) G. Barkhordarian, T. Klassen, R. Bormann, *US Patent App. 11/721,493*, **2009**.

- [2] a) T.-T. Le, C. Pistidda, J. Puszkiel, M. V. Castro Riglos, F. Karimi, J. Skibsted, S. P. GharibDoust, B. Richter, T. Emmler, C. Milanese, A. Santoru, A. Hoell, M. Krumrey, E. Gericke, E. Akiba, T. R. Jensen, T. Klassen, M. Dornheim, *J. Phys. Chem. C* **2018**, 122, 7642; b) P. K. Pranzas, U. Bösenberg, F. Karimi, M. Munning, O. Metz, C. B. Minella, H.-W. Schmitz, F. Beckmann, U. Vainio, D. Zajac, E. Welter, T. R. Jensen, Y. Cerenius, R. Bormann, T. Klassen, M. Dornheim, A. Schreyer, *Adv. Eng. Mater.* **2011**, 13, 730; c) F. Karimi, M. V. C. Riglos, A. Santoru, A. Hoell, V. S. Raghuvanshi, C. Milanese, N. Bergemann, C. Pistidda, P. Nolis, M. D. Baro, G. Gizer, T.-T. Le, P. K. Pranzas, M. Dornheim, T. Klassen, A. Schreyer, J. Puszkiel, *J. Phys. Chem. C* **2018**, 122, 11671.
- [3] H. B. Stuhmann, *Q. Rev. Biophys.* **1981**, 14, 433.
- [4] a) F. Karimi, P. K. Pranzas, J. A. Puszkiel, M. V. Castro Riglos, C. Milanese, U. Vainio, C. Pistidda, G. Gizer, T. Klassen, A. Schreyer, M. Dornheim, *RSC Adv.* **2021**, 11, 23122; b) J. A. Puszkiel, M. V. Castro Riglos, J. M. Ramallo-López, M. Mizrahi, F. Karimi, A. Santoru, A. Hoell, F. C. Gennari, P. A. Larochette, C. Pistidda, T. Klassen, J. M. Bellosta von Colbe, M. Dornheim, *J. Mater. Chem. A* **2017**, 5, 12922.
- [5] a) T. T. Le, C. Pistidda, V. H. Nguyen, P. Singh, P. Raizada, T. Klassen, M. Dornheim, *Int. J. Hydrogen Energy* **2021**, 46, 23723; b) T. T. Le, C. Pistidda, C. Abetz, P. Georgopoulos, S. Garroni, G. Capurso, C. Milanese, J. Puszkiel, M. Dornheim, V. Abetz, T. Klassen, *Materials* **2020**, 13, 991.
- [6] a) Z. Ding, H. Li, L. Shaw, *Chem. Eng. J.* **2020**, 385, 123856; b) F. Karimi, M. V. C. Riglos, A. Santoru, A. Hoell, V. S. Raghuvanshi, C. Milanese, N. Bergemann, C. Pistidda, P. Nolis, M. D. Baro, G. Gizer, T.-T. Le, P. K. Pranzas, M. Dornheim, T. Klassen, A. Schreyer, J. Puszkiel, *J. Phys. Chem. C* **2018**, 122, 11671.
- [7] S. Börries, O. Metz, P. K. Pranzas, T. Bücherl, S. Söllradl, M. Dornheim, T. Klassen, A. Schreyer, *Nucl. Instrum. Methods Phys. Res. Sect. A* **2015**, 797, 158.
- [8] S. Börries, O. Metz, P. Pranzas, J. B. von Colbe, T. Bücherl, M. Dornheim, T. Klassen, A. Schreyer, *J. Power Sources* **2016**, 328, 567.
- [9] I. Manke, H. Markötter, C. Tötze, N. Kardjilov, R. Grothausmann, M. Dawson, C. Hartnig, S. Haas, D. Thomas, A. Hoell, C. Genzel, J. Banhart, *Adv. Eng. Mater.* **2011**, 13, 712.
- [10] G. K. Batchelor, *An Introduction to Fluid Dynamics*, Cambridge University Press, Cambridge **2000**.
- [11] C. Hall, W. D. Hoff, *Water Transport in Brick, Stone and Concrete*, CRC Press, Boca Raton, FL **2011**.
- [12] J. Jepsen, PhD thesis, Helmut-Schmidt Universität, Hamburg **2013**.
- [13] U. Bösenberg, C. Pistidda, M. Tolkieln, N. Busch, I. Saldan, K. Suarez-Alcantara, A. Arendarska, T. Klassen, M. Dornheim, *Int. J. Hydrogen Energy* **2014**, 39, 9899.
- [14] A. H. H. Bieder, L. Mokrani, I. Zizak, *Patent*, **2007**.
- [15] A. Hoell, D. Tatchev, S. Haas, J. Haug, P. Boesecke, *J. Appl. Crystallogr.* **2009**, 42, 323.
- [16] G. Goerigk, K. Huber, N. Mattern, D. L. Williamson, *Eur. Phys. J. Spec. Top.* **2012**, 208, 259.
- [17] D. Svergun, *J. Appl. Crystallogr.* **1992**, 25, 495.
- [18] D. Bellmann, P. Staron, P. Becker, *Phys. B* **2000**, 276–278, 124.
- [19] P. Staron, D. Bellmann, *J. Appl. Crystallogr.* **2002**, 35, 75.
- [20] M. Dierick, B. Masschaele, L. V. Hoorebeke, *Meas. Sci. Technol.* **2004**, 15, 1366.
- [21] V. G. GmbH, *Vgstudio max*, <https://www.volumegraphics.com/de/produkte/vgstudio-max/basic-edition.html>